Dislocation engineering in SiGe on periodic and aperiodic Si(001) templates studied by fast scanning X-ray nanodiffraction

Valeria Mondiali,[1] Monica Bollani,[2,a)] Stefano Cecchi,[1] Marie-Ingrid Richard,[3,4] Tobias Schülli,[3] Gilbert Chahine,[3] and Daniel Chrastina[1]
[1]*L-NESS, Dipartimento di Fisica, Politecnico di Milano, Polo di Como, via Anzani 42, 22100 Como, Italy*
[2]*IFN-CNR, L-NESS, via Anzani 42, 22100 Como, Italy*
[3]*ID01/ESRF, BP 220, F-38043 Grenoble Cedex, France*
[4]*Aix-Marseille Université, CNRS, IM2NP UMR 7334, Campus de St Jérôme, F-13397 Marseille Cedex, France*

(Received 28 November 2013; accepted 7 January 2014; published online 17 January 2014)

Fast-scanning X-ray nanodiffraction microscopy is used to directly visualize the misfit dislocation network in a SiGe film deposited on a pit-patterned Si substrate at the beginning of plastic relaxation. X-ray real-space diffracted intensity maps are compared to topographic atomic force microscopy images, in which crosshatch lines can be seen. The change in intensity distribution as a function of the incidence angle shows localized variations in strain within the SiGe film. These variations, which reflect the order imposed by the substrate pattern, are attributed to the presence of both bunches of misfit dislocations and defect-free regions. © *2014 AIP Publishing LLC*. [http://dx.doi.org/10.1063/1.4862688]

The adoption of SiGe/Si structures by the information and communications technology industries has been limited to relatively thin layers, for example, within heterojunction bipolar transistors,[1] or as local stressors for strained Si channel transistors.[2] The possibility of using thicker SiGe layers, for example, in detectors is hindered by the nucleation of misfit dislocations associated with the plastic relaxation of the material. Misfit dislocations impact negatively on device performance,[3] and the random nature of the nucleation process means that the device yield becomes unpredictable. Methods of reducing or controlling the distribution of misfit dislocations may, therefore, extend the applications of SiGe/Si structures as well as offering new ways of studying the mechanisms of dislocation formation.

It has been shown that epitaxial deposition of a low-misfit $Si_{1-x}Ge_x$ film on top of a Si (001) substrate patterned with {111}-faceted pits oriented in a square network along the ⟨110⟩ directions leads to the trapping of misfit dislocations.[4] The patterning strongly influences the nucleation and the propagation of dislocations during the onset of plastic relaxation, preferentially gettering misfit segments along pit rows. This behavior has been explained in terms of an energy minimization for 60° misfit dislocation segments located at the (111) interface.[5]

To better understand this effect, thin Si-rich SiGe films have been deposited on periodic and aperiodic templates fabricated on Si (001) substrates. Both p-type and n-type Si substrates used are in the same resistivity range (1–10 Ω cm), and the doping did not show any impact on the dislocation engineering processes. The aperiodic pattern is aimed to evaluate, within a single sample, the influence of pit spacing on the nucleation of misfit dislocations. All the samples have been characterized by scanning electron microscopy (SEM) and atomic force microscopy (AFM) to analyze the surface morphology and to confirm that the pit pattern controls the propagation of the misfit dislocations along the [110] and [1$\bar{1}$0] directions. Moreover, diffraction experiments were performed using a nano-focused X-ray beam at the ID01 beamline of the European Synchrotron Radiation Facility in Grenoble (France). Using quic**K** continuous **Map**ping (K-Map),[6,7] diffraction intensity maps in real space have been obtained and compared with surface topography maps realized by laboratory AFM. By simultaneously combining high-speed continuous motion of the positioning system with high frequency image recording, the K-Map method allows 2-dimensional diffraction intensity maps to be obtained extremely quickly as compared to the previously used method of step-wise scanning, detector image acquisition, and reconstruction.[8] Therefore, immediate identification and quick localization of epitaxial nanostructures may be achieved in detail.

In this work, we show how the diffraction intensity maps are sensitive to the bunches of dislocations, which propagate between lithographically defined {111} pits, typically observed by AFM or transmission electron microscopy (TEM). In order to control the formation and propagation of misfit dislocations during the deposition of the SiGe film, the Si (001) substrate, covered with a 100 nm of SiN_x layer (Fig. 1(a)), is patterned with arrays of {111}-faceted pits aligned along the ⟨110⟩ directions. The pits grid was defined by electron beam lithography (EBL), so that periodic and aperiodic patterns could be defined. The periodic pattern featured a pit pitch of 2.5 μm, while the aperiodic pattern was designed with a pit pitch increasing from 2 to 5 μm in steps of 1 μm. These patterns were transferred into the nitride layer by reactive ion etching (RIE) to define a hard mask (Fig. 1(b)). Pits with the shape of inverted {111}-faceted pyramids were then formed by anisotropic wet etching of the Si substrate with tetramethylammonium hydroxide (TMAH) at 80 °C for 6 min (Fig. 1(c)).[9] For the samples reported in this work, the

a)Author to whom correspondence should be addressed. Electronic mail: monica.bollani@ifn.cnr.it.

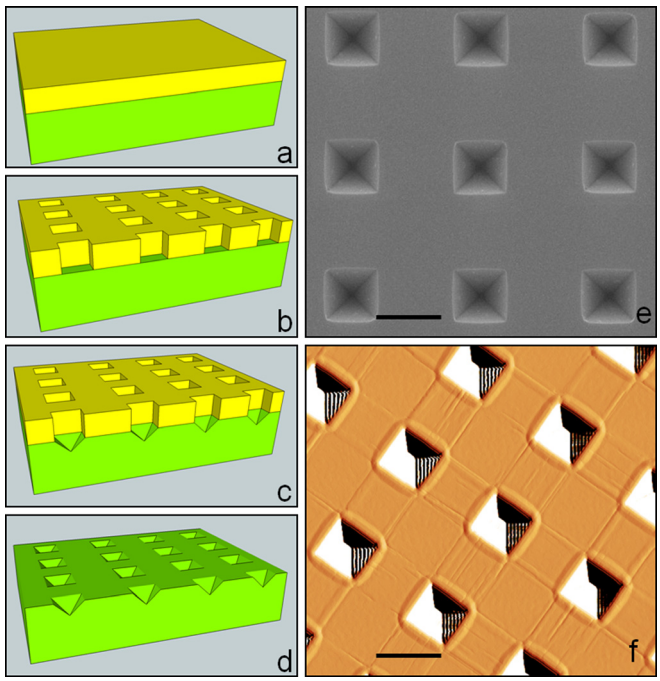

FIG. 1. (a)–(d) A schematic sequence of the fabrication steps for inverted pyramids on a Si (001) substrate, where the thicknesses and the pit size are not in scale. In (a) 100 nm of SiN_x is deposited by sputtering. By electron beam lithography and reactive ion etching, a mask with square openings is defined (b). By wet chemical anisotropic etching, inverted pyramids are obtained with an angle of 54.7° between the (111) and the (001) planes (c), and finally, the SiN_x film is removed by phosphoric acid solution (d). (e) SEM image of a symmetrical pattern made up of an array of inverted {111}-faceted pyramids before deposition of the SiGe layer. The pitch is 2.5 μm, the distance between the inverted pyramids is about 1.5 μm and the pyramid width is about 1 μm. (f) AFM tapping amplitude image of a symmetrical pattern made up of an array of inverted {111}-faceted pyramids after the deposition of a 250 nm thick $Si_{0.8}Ge_{0.2}$ layer. The image area is about $10 \times 10\ \mu m^2$. The lines connecting the pits are attributed to bunches of misfit dislocations at the Si/SiGe interface. For AFM imaging ultra sharp tips were used. According to the surface topography, misfit dislocations run along pit rows while the regions between rows remain dislocation free. The scale bar for images (e) and (f) is 2 μm long.

typical width of the pits after etching was 1 μm with a corresponding depth of 600 nm. After the hard mask removal by phosphoric acid at 180 °C (Fig. 1(d)), the patterned substrates were cleaned by a standard RCA treatment. The SEM image in Fig. 1(e) shows part of a patterned substrate, where a typical matrix of fully etched inverted {111} pits on a Si (001) substrate surface is achieved. Before each deposition, the substrates were dipped in dilute hydrofluoric acid and rinsed in water to remove the native oxide and create a hydrogen terminated surface, before loading into the low-energy plasma-enhanced chemical vapor deposition (LEPECVD) growth system.[10] Then, a 45 nm Si buffer and a 250 nm $Si_{1-x}Ge_x$ alloy layer (with a Ge content x of 16%–20%) were deposited at 700 °C with a growth rate of about 0.38 nm/s. In this way, a continuous SiGe film, which follows the same topography as the patterned substrate, is achieved, as shown in Fig. 1(f). During the deposition of a SiGe film on Si, the relaxation of the SiGe alloy is limited by the rates of dislocation nucleation and multiplication.[11,12] For the samples studied in this work, although the film is well above the equilibrium critical thickness for relaxation (13–20 nm in this range of Ge content), the layers are expected to relax only slightly since these conditions correspond to only the beginning of dislocation nucleation.[13] For the aperiodic and periodic patterns studied in this work, the Ge content x is ~16% and ~20%, while the degree of relaxation, β, is ~3.5% and ~12%, respectively, as found by laboratory X-ray diffraction measurements around the (004) and (224) Bragg peaks. Considering that the Burgers vector length $b = a(x)/\sqrt{2}$ is about 0.4 nm (where $a(x)$ is the alloy lattice parameter), and that the misfit f is approximately $0.04x$, the average 60° misfit spacing can be estimated as $b/(2\beta|f|)$ and corresponds to 60° misfit spacings of 0.9 and 0.2 μm, respectively, for 16% and 20% Ge content at the degrees of relaxation given above.

Figure 1(f) shows a tapping mode AFM image of a periodic pattern with 1 μm wide and 600 nm deep pits with a pitch of 2.5 μm: The lines connecting the corners of the pits are attributed to the bunches of misfit dislocations, which propagate along pit rows.[14] The pit pattern produces an inhomogeneous stress distribution in the SiGe film: The high strain sites are the preferential sites for dislocation nucleation in terms of energy minimization. This happens as long as the degree of relaxation does not require the misfit network to be much denser than the pit spacing.[4] If this condition is fulfilled, the misfit dislocations segments run between the pits rather than randomly through the layer. This leads to dislocation-free regions between pit rows, as shown in Fig. 1(f). Figure 2(a) shows an AFM tapping amplitude overview of the aperiodic pattern. The distribution of surface crosshatch lines indicates the presence of bunches of dislocations that propagate along the pit rows. The patterned area is about $60 \times 60\ \mu m^2$, which fits within the $100 \times 100\ \mu m^2$ range of the x and y piezo scanning stage available at the ID01 beamline. In Fig. 2(b), a $20 \times 20\ \mu m^2$ scan corresponding to the area marked in Fig. 2(a) is shown.

TEM analyses would normally be required to verify the correlation between surface crosshatch lines and misfit dislocations at the SiGe/Si interface. However, TEM is a destructive technique, for which sample preparation is rather difficult, especially for thin layers or nanostructures.[15] The Fast-scanning X-ray nanodiffraction microscopy technique offers a non-destructive technique to access to structural properties (strain, lattice orientation) with sub-micrometer resolution without need of sample preparation and without any surface or morphological limitations (buried films or integrated circuits), and the required experimental setups are increasingly becoming available at synchrotron light sources.[7,8] Moreover, a significant gain of time compared to classical X-ray scanning methods is obtained: up to eight decades in the acquisition time of two-dimensional scans. Finally, the approach clearly opens new experimental possibilities such as *in situ* experiments (e.g., following in real time the structural evolution during heating, catalytic reaction, magnetic/electric field exposition, etc.). In the present work, the misfit lines are directly visible under appropriate diffraction conditions due to the local lattice tilts and alloy composition variations associated with their strain fields.[16,17] The ultimate aim of the nanodiffraction analysis is to understand the relationship between pit spacing, layer thickness, and homogeneity of strain relaxation, in order to obtain strain-relaxed areas, which are free of dislocations.

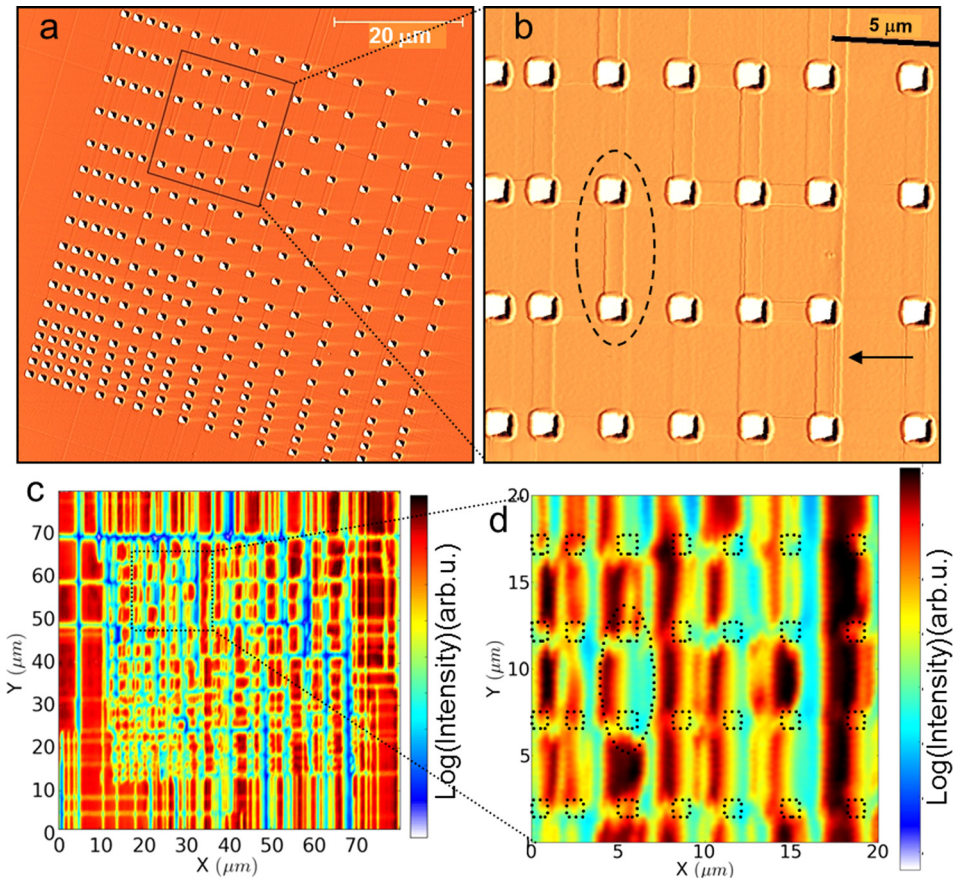

FIG. 2. (a) AFM tapping amplitude image of an aperiodic pattern made up of an array of inverted {111}-faceted pyramids on top, which a 250 nm thick $Si_{0.85}Ge_{0.15}$ layer was deposited. The pitch increases from 2 to 5 μm. The patterned area is about $60 \times 60\ \mu m^2$. A $20 \times 20\ \mu m^2$ square marks the area shown in (b), where the lines between the pits, corresponding to bunches of dislocations, can clearly be seen. (c) X-ray diffraction intensity real space map taken at the (113) Bragg condition of the SiGe film over the same area analyzed by AFM in (a): the same features can be identified in both (a) and (c), both within and outside the aperiodic pattern itself. In particular, apart from the pits themselves, crosshatch lines in the AFM image correspond to regions of lower intensity in the X-ray map. (d) X-ray map of the same area of (b) at the SiGe (113) Bragg conditions, with the pit positions marked as a guide to the eye. The feature marked with the dotted oval corresponds perfectly between the two images. In all experiments, the X-ray beam is incident from the right of the image, and the detector is on the left. The x direction is therefore defined to be [110], and the diffraction measurement is only sensitive to in-plane strain in this direction not the $[1\bar{1}0]$ direction.

Nanodiffraction experiments were carried out at a beam energy of 8.47 keV, so that the (004) and (113) Bragg peaks were accessible at a scattering angle, $2\theta_{Bragg}$, of about 65° and 53°, respectively, with θ_{Bragg} being the Bragg angle. The latter was accessed in grazing-exit geometry in order to maintain a small incident spot size on the sample (incidence angle $\omega \sim 52°$). The very low exit angle ($\sim 1°$) means that the diffracted intensity is concentrated close to the surface of the sample, thereby minimizing the brightness of the Si substrate peak. The incident beam was focused to a 250×750 nm^2 (vertical × horizontal) spot size using a Fresnel zone plate of 300 μm diameter and 80 nm outer-most zone width,[18] leading to a beam footprint on the sample of $\sim 320 \times 750$ nm^2 at the given (113) incidence angle. The diffracted beam was recorded with a two-dimensional MAXIPIX photon-counting detector,[19] characterized by 516×516 pixels and 55 μm pixel size, and positioned at 1.26 m from the sample. Regions of interest (ROIs) close to the Si and SiGe Bragg peaks were defined on the detector, so that during the measurements, the integrated intensity over these ROIs was recorded. The sample was mounted on a fast xyz scanning piezoelectric stage, with a lateral stroke of 100 μm and a resolution of 2 nm. It was itself mounted on a hexapod. An optical microscope was mounted on the goniometer, rotating with the sample, so that patterned regions could be found and positioned in the path of the X-ray beam.

The intensity map shown in Fig. 2(c) represents a two-dimensional real-space map of the total diffracted intensity of the SiGe (113) Bragg peak, in which the aperiodic pattern shown in Fig. 2(a) can clearly be identified. A total area of $80 \times 80\ \mu m^2$ was scanned by tiling 16 scans of $20 \times 20\ \mu m^2$ each. The crosshatch lines in the AFM image due to pile-ups of misfit dislocations correspond to regions of lower intensity in the X-ray map, represented in blue in Fig. 2(c). The excellent match between the morphological and intensity maps clearly proves that the strain field induced by the dislocations can be qualitatively observed by the fast scanning X-ray nano-diffraction measurement. Since the Bragg peak was aligned in an unpatterned region of the sample, this can be considered as a "bright field" image: In this case, the dislocation lines (which correspond to crosshatch lines visible in AFM images) result in a loss of diffracted intensity. Figure 2(d) displays an X-ray map of the same area as in Fig. 2(b), around the SiGe (113) Bragg peak, with the pit positions

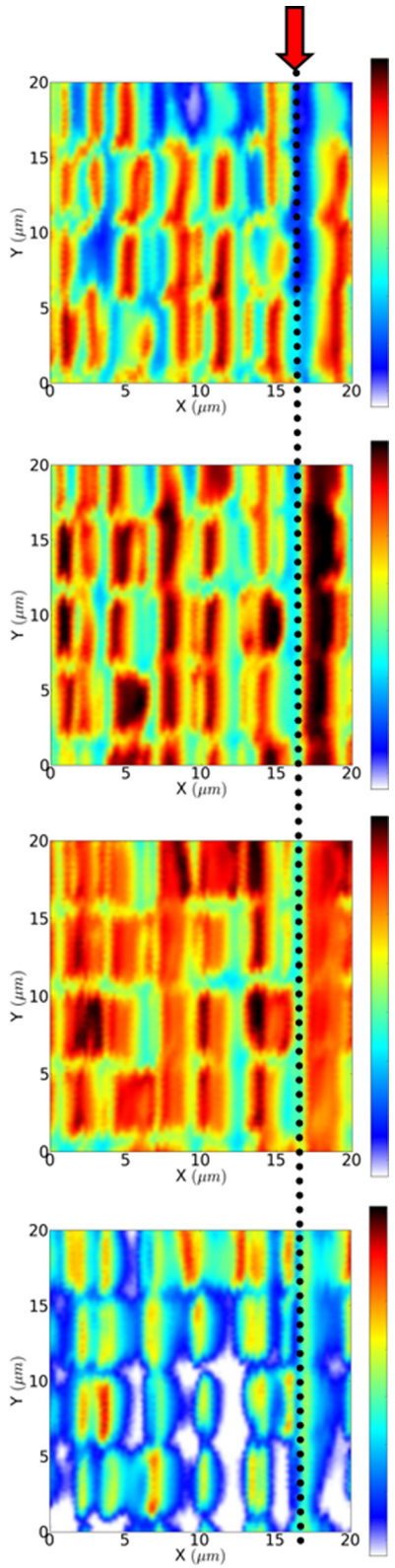

FIG. 3. X-ray intensity maps corresponding to the same region as in Fig. 2(d), taken at incidence angles of, from top to bottom, $\Delta\omega = -0.02°$, $0.00°$, $+0.03°$, and $+0.08°$ with respect to the SiGe (113) Bragg condition. A vertical dotted line marks the position of a line defect, which is visible at positive $\Delta\omega$, corresponding to locally increased strain with respect to the SiGe layer. This line is marked with an arrow in Fig. 2(b). The color scale indicates the logarithm of the intensity, increasing from blue to red.

marked as a guide to the eye. The feature marked with the dotted oval shows the perfect correspondence between the two images. The color maps denote the presence of regions with different relaxation levels: the blue color represents a relaxed area that corresponds to the dislocation lines visible also in AFM images. The red–yellow zones between the pits correspond to strained areas, which are not affected by plastic relaxation. The X-ray beam is incident from the right of the image, and the detector is on the left, so the x direction is defined to be [110]. The symmetric (004) diffraction measurement is sensitive only to the out-of-plane lattice parameter along [001], but the asymmetric (113) measurement is sensitive to the in-plane strain along [110] but not $[1\bar{1}0]$. (The measurement is only sensitive to lattice plane tilting in the $[1\bar{1}0]$ direction, leading to non-coplanar diffraction.) This means that the measurement is only sensitive to the in-plane strain fields of misfits running in the $[1\bar{1}0]$ direction, as labeled by the red arrow in Fig. 3. The arrow and the dotted line in Figs. 2(b) and 2(d) are used as reference for Fig. 3. These X-ray intensity maps show how the total diffracted intensity changes as the incidence angle is moved slightly away from the Bragg condition. Intensity at slightly lower incidence angles corresponds to an increase in the degree of relaxation (less strain), and vice versa. So, by considering the variation of intensity for the different images, a qualitative sense of the strain variation corresponding to defects can be built up. Areas, which present high intensity at a single incidence angle, are defect-free with a well-defined strain state. These dislocation-free regions may be homogeneously strained and suitable for device growth. Some areas can be identified which are brighter in the image at $+0.03°$, compared to the Bragg condition, indicating increased strain within the pattern. Defect lines can also be identified, showing diffracted intensity over a broader range of incidence angles away from the Bragg peak. Bright horizontal lines are not seen in any images, since the defects running in this direction induce lattice tilts, which cause the diffracted X-ray beam to leave the coplanar scattering geometry condition.

In conclusion, this work shows how a fast-scanning X-ray measurement can be used to study the propagation of misfit dislocation bunches formed during the epitaxial growth of SiGe films on pre-patterned Si substrates. The use of a Si-rich SiGe layer, at the very beginning of relaxation, ensures that the misfit network is relatively sparse. It is found that the obtained X-ray maps qualitatively reflect the AFM topographical images.

We acknowledge the Cariplo Foundation (within the grant DefCon4 2011-0331) for partial financial support.

[1]S. C. Jain, S. Decoutere, M. Willander, and H. E. Maes, Semicond. Sci. Technol. **16**, R51 (2001); Sci. Technol. **16**, R67 (2001).
[2]S. E. Thompson, G. Sun, Y. S. Choi, and T. Nishida, IEEE Trans. Electron Devices **53**, 1010 (2006).
[3]J. G. Fiorenza, G. Braithwaite, C. W. Leitz, M. T. Currie, J. Yap, F. Singaporewala, V. K. Yang, T. A. Langdo, J. Carlin, M. Somerville, A. Lochtefeld, H. Badawi, and M. T. Bulsara, Semicond. Sci. Technol. **19**, L4 (2004).
[4]M. Grydlik, F. Boioli, H. Groiss, R. Gatti, M. Brehm, F. Montalenti, B. Devincre, F. Schäffler, and L. Miglio, Appl. Phys. Lett. **101**, 013119 (2012).
[5]R. Gatti, F. Boioli, M. Grydlik, M. Brehm, H. Groiss, M. Glaser, F. Montalenti, T. Fromherz, F. Scäffler, and L. Miglio, Appl. Phys. Lett. **98**(12), 121908 (2011).

[6]G. Chahine, M.-I. Richard, R. A. Homs, T.-N. Tran-Caliste, D. Carbone, V. L. R. Jacques, R. Grifone, P. Boesecke, H. Djazouli, I. Costina, J. Katzer, T. Schroeder, and T. U. Schülli, "Imaging of strain and lattice orientation by quick scanning x-ray microscopy combined with 3D reciprocal space mapping," J. Appl. Crystallogr. (submitted).
[7]T. Etzelstorfer, M. J. Süess, G. L. Schiefler, V. L. R. Jacques, D. Carbone, D. Chrastina, G. Isella, R. Spolenak, J. Stangl, H. Sigg, and A. Diaz, J. Synchrotron Radiat. **21**, 111 (2014).
[8]D. Chrastina, G. M. Vanacore, M. Bollani, P. Boye, S. Schöder, M. Burghammer, R. Sordan, G. Isella, M. Zani, and A. Tagliaferri, Nanotechnology **23**, 155702 (2012).
[9]K. Sato, M. Shikida, T. Yamashiro, K. Asaumi, Y. Iriye, and M. Yamamoto, Sens. Actuators, A **73**, 131 (1999).
[10]G. Isella, D. Chrastina, B. Rössner, T. Hackbarth, H.-J. Herzog, U. König, and H. von Känel, Solid-State Electron. **48**, 1317 (2004).
[11]R. People and J. C. Bean, Appl. Phys. Lett. **47**, 322 (1985).
[12]R. Hull, J. C. Bean, D. J. Werder, and R. E. Leibenguth, Appl. Phys. Lett. **52**, 1605 (1988).
[13]R. Beanland, J. Appl. Phys. **72**, 4031 (1992).
[14]A. Fischer, H. Kühne, M. Eichler, F. Holländer, and H. Richter, Phys. Rev. B **54**, 8761 (1996).
[15]K. Usuda, T. Numata, T. Irisawa, N. Hirashita, and S. Takagi, Mater. Sci. Eng., B **124–125**, 143 (2005).
[16]L. Martinelli, A. Marzegalli, P. Raiteri, M. Bollani, F. Montalenti, L. Miglio, D. Chrastina, G. Isella, and H. von Känel, Appl. Phys. Lett. **84**, 2895 (2004).
[17]I. N. Remediakis, D. E. Jesson, and P. C. Kelires, Phys. Rev. Lett. **97**, 255502 (2006).
[18]S. Gorelick, J. Vila-Comamala, V. A. Guzenko, R. Barrett, M. Salomé, and C. David, J. Synchrotron Radiat. **18**, 442 (2011).
[19]C. Ponchut, J. M. Rigal, J. Clément, E. Papillon, A. Homs, and S. Petitdemange, J. Instrum. **6**, C01069 (2011).